Fischbacher, Richard Bernd, BSc.

Modeling of Parasitic Capacitive Coupling to HF RFID Sensor Tags

Master Thesis

to achieve the university degree of

Master of Science

Master's degree programme: Electrical Engineering

submitted to

Graz University of Technology

Supervisor:

Grosinger, Jasmin, Ass.Prof. Dipl.-Ing. Dr.techn. BSc.

Co-Supervisor:

Landauer, Gerhard, Dipl.-Ing. Dr., NXP Semiconductors Austria GmbH

Institute for Microwave and Photonic Engineering

Head: Bösch, Wolfgang, Univ.-Prof. Dipl.-Ing. Dr.techn. MBA

Graz, Oktober 2018

Affidavit

I declare that I have authored this thesis independently, that I have not used other than the declared sources/resources, and that I have explicitly indicated all material which has been quoted either literally or by content from the sources used. The text document uploaded to TUGRAZonline is identical to the present master's thesis.

Date	Signature

Acknowledgments

Hereby I want to thank everyone who did support me during my academic studies and especially during my Master Thesis.

A special thanks goes out to my parents, Richard and Maria who never stopped supporting me during my whole education.

Furthermore, I would like to thank Jasmin Grosinger, Gerhard Landauer, Ivan Rebollo, Lukas Görtschacher, and Franz Amtmann for their time, effort, continuous support, weekly feedback and amazing input throughout my whole Master Thesis.

Richard Bernd Fischbacher

Abstract

In this thesis, I investigate parasitic capacitive coupling between high frequency (HF) radio frequency identification (RFID) reader antennas and capacitive sensing elements attached to HF RFID passive sensor transponders. I create a circuit model (CM) to efficiently model the electrical behavior of the reader antenna, the capacitive coupling network, and the sensing element. A CM is beneficial, in particular for analog circuit designers of sensor transponder microchips, because the model gives a significant insight into the characteristics of parasitic capacitive coupling and can be implemented easily in a circuit simulation environment.

First, a general CM for a coil is introduced and is verified by measurements and electromagnetic simulations. The comparison of CM, measurement, and simulation results verifies additionally the electromagnetic simulation environment. Next, a capacitive coupling network is chosen to model the parasitic capacitive coupling between the reader antenna and the sensing element. It has been shown that a simple network is sufficiently accurate to model the coupling effects. The benefit of such a simple network is that it allows a time-efficient calculation of the parasitic coupling of the reader-sensor tag system. The lumped components of the simple CM are determined by comparing the input and transmission impedances of the CM and the created electromagnetic model of the complete system. In particular, the input and transmission impedances at the defined input ports are optimized for specific realistic geometries of the reader coil and the capacitive sensing element. After this first optimization, the capacitances of the CM are fine-tuned in a small range of capacitance values by

additionally optimizing the transmission impedances, which leads to a good overall alignment of CM and electromagnetic simulation model and a very good transmission impedances alignment at the HF RFID operating frequency of 13.56 MHz with a difference of less than 1 %.

Contents

1 Introduction

Many automatic identification procedures have been developed in the past. A few examples are: bar-codes, optical character recognition, biometric procedures, and radio frequency identification (RFID) [8]. Generally speaking, RFID has proven to be more versatile than the alternative identification systems in the same price class, therefore its global sales are rising each year [8]. Thus, a lot of effort is put into the research of different applications for RFID systems. An RFID system consists of a reader and a transponder (tag) [8]. A reader is a device, which is used to read out data from a tag. A tag consists of a tag microchip (chip) and an antenna, which is used for communication with the reader. The reader and tag antenna are, in the case of high frequency (HF) RFID on which this thesis does focus on, two weakly coupled coils [1]. Furthermore, low-end tags typically operate passively, which means that they have not an energy source of their own and that they are supplied by the magnetic field of the reader, similar to a transformer.

Generally speaking, tags store data, e.g., an identification number (ID). Furthermore, developments also introduced tags with built-in sensors, which could return, e.g., a simple binary sensing state. The chip has an integrated sensor interface that is connected to the sensing element. Such a sensing element could be, for example, a wire loop. The binary state then distinguishes between a closed wire loop and an open wire loop, i.e., causing a short circuit or an open circuit between a detection pin and the ground of the tag [16]. The detection of this binary state does experience disturbances due to parasitic coupling between the reader antenna and the wire loop. The wire loop couples

inductively with the reader antenna in case of the short circuit and couples capacitively with the reader antenna in case of the open circuit. In Sec. 1.2.1, the disturbances due to parasitic capacitive coupling are estimated to be even larger than the disturbances due to parasitic inductive coupling. Thus, it is especially important to explore parasitic capacitive coupling effects of reader antennas to capacitive sensing elements attached to chips. In this thesis, the sensing element is an external capacitive sensing elements. This is an important fact, because until now, most published research is currently dealing with capacitive on-chip sensing elements, which have the benefit of being smaller in size and thus being less vulnerable to parasitic capacitive coupling ([10], [5], [2]).

This thesis investigates and models the effects of parasitic capacitive coupling of reader antennas and external capacitive sensing elements. In particular, this thesis is aimed to model these disturbances. This is important for circuit designers of microchips that have to deal with these disturbances to create disturbance-robust chips. This is the reason why the goal of this thesis is to introduce a circuit model (CM) to efficiently model the electrical behavior of parasitic capacitive coupling from HF RFID reader antennas to capacitive sensing elements of HF RFID sensor tags as accurate and simple as possible. The developed CM can then be used in circuit-level simulations to support the design of disturbance-robust sensor tags.

1.1 HF RFID Systems

In this section the basic principles of HF ($f = 13.56\,\text{MHz}$ [8]) RFID systems with passive sensor tags are summarized. For passive tags inductive coupling is utilized, to supply them with energy and to establish communication with

the reader over the magnetic field of the reader (see Fig.1.1). The carrier wavelength λ[1] (22.1 m at 13.56 MHz) is several times greater than the operating range of these tags, which is why the magnetic field can be treated as a simple alternating magnetic field instead of requiring the consideration of wave propagation [8].

1.1.1 Antenna Characteristics

All considerations assume that the tag is in the near field of the reader, which means that the distance between tag antenna and reader antenna is lower than $0.16 \cdot \lambda$. If moved farther away, backscatter coupling effects have to be taken into account [8].

Coupling Mechanism

The inductive coupling between two coils can be described with the coupling coefficient k and the mutual inductance M. Here, M_{rt} is the mutual inductance between the reader and the tag, I_t the current through the tag antenna, I_r the current through the reader antenna, $\psi_r(I_r)$ the magnetic flux created by I_r, $\psi_t(I_r)$ the magnetic flux through the tag antenna caused by I_r, $B_t(I_r)$ the magnetic field passing through the tag antenna caused by I_r, N_t the number of coil turns and A_t the area of the loop of the tag antenna. By estimating $B_t(I_r)$ analytically and being aware of the antenna characteristics, the mutual inductance between two antennas can be estimated by:

$$M_{rt} = \frac{\psi_t(I_r)}{I_r} = \frac{B_t(I_r) \cdot N_t \cdot A_t}{I_r}, \tag{1.1}$$

which is necessary for Sec. 2.5 [8].
In Fig. 1.1, I_r, I_t, $\psi_t(I_r)$, $\psi_r(I_r)$, and $B_t(I_r)$ are illustrated for a generic reader-

[1] $\lambda = \frac{c}{f}$

tag setup. Further, by knowing M_{rt} from 1.1, L_r the reader antenna inductance,

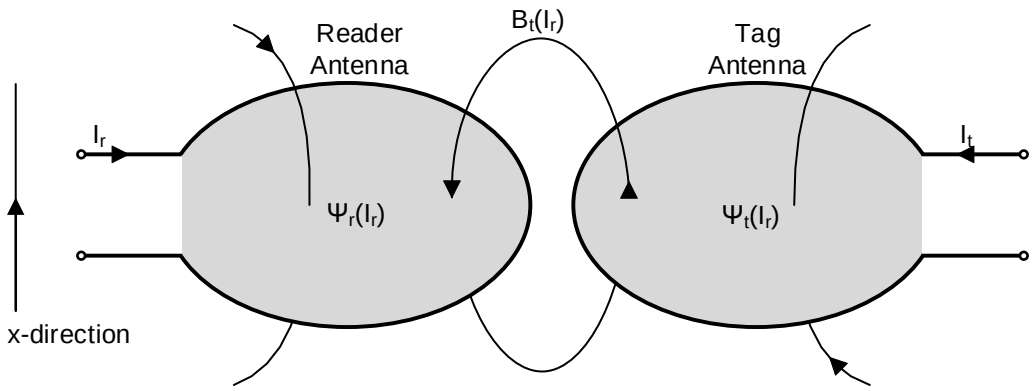

Figure 1.1: Field properties relevant for inductive coupling [8]: This figure illustrates the shared magnetic flux and magnetic field between the reader and tag antenna. In addition, the directions of the magnetic field quantities and reader and tag current are presented.

and L_t the tag antenna inductance, k can be calculated with [8]:

$$k = \frac{M_{rt}}{\sqrt{L_r \cdot L_t}}. \tag{1.2}$$

Magnetic Field

In a first approximation and under the assumption of the height of the coil being much smaller than the diameter, the magnetic field in the near field of a single cylindrical coil in x-direction (see Fig. 1.1) can be described with [8]:

$$H = \frac{I \cdot N \cdot r^2}{2 \cdot \sqrt{(r^2 + x^2)^3}}. \tag{1.3}$$

Here, r is the radius of the coil, H[2] the magnetic field strength, I the current through the coil, N the number of coil turns, and x the distance in x-direction (see Fig.1.1). In Figure 1.2 the $\frac{1}{x}$ proportionality of the magnetic field with respect to the distance in x direction is shown. This mathematical example results in an attenuation of roughly 100 dB in the near field of the reader. One has to keep in mind that this attenuation is only present for the tag if its operating range is 3.57 m. Due to this large dynamic range a voltage regulator has to be included into the chips analog front-end to keep the voltage in its boundaries given by the respective semiconductor technology. This can be realized with, e.g., a voltage-dependent shunt resistor [8].

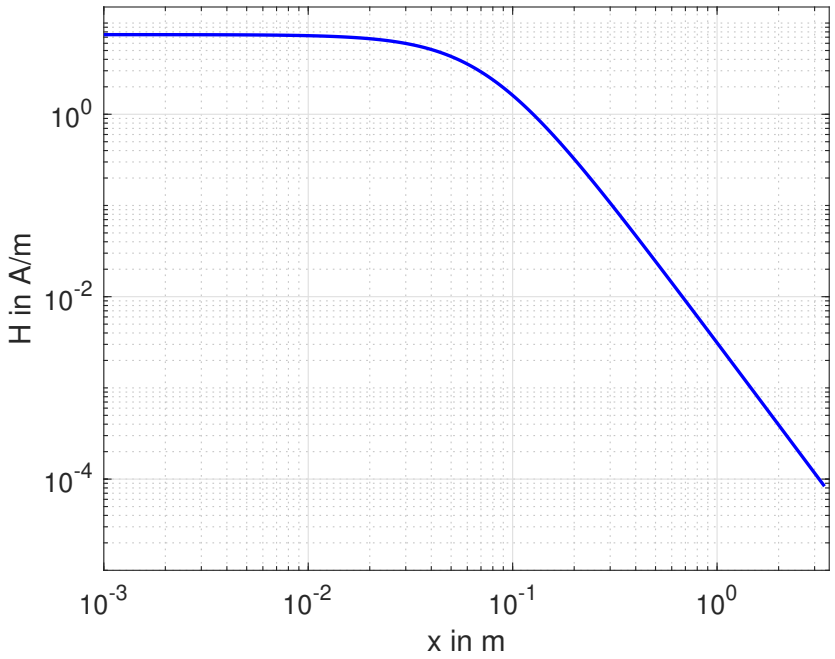

Figure 1.2: Magnetic field strength (H) of a reader coil versus x (see Fig. 1.1, $I = 0.1\,\text{A}$, $N = 5$, $r = 3\,\text{cm}$): The influences of a tag in the near field of the reader antenna are not shown in this graph.

[2] $B = \mu \cdot H$ with μ being the permeability [8].

Resonance

The antenna inductance L_r and parallel capacitance C_r (see Fig. 1.3) are forming a parallel resonant circuit. These elements are usually tuned to have a resonance frequency of 13.56 MHz. This results, due to resonance step-up, in the generation of a high current to boost the intensity of the magnetic.
The induced voltage u_t in the tag antenna is calculated with the formula (see Fig. 1.3) [8]:

$$u_t = \frac{\omega \cdot k \cdot \sqrt{L_r \cdot L_t} \cdot I_r}{\sqrt{(\frac{\omega \cdot L_t}{R_L} + \omega \cdot R_t \cdot C_t)^2 + (1 - \omega^2 \cdot L_t \cdot C_t + \frac{R_t}{R_L})^2}}. \tag{1.4}$$

Here, ω[3] is the angular frequency, I_r the current through the reader antenna, R_L the load resistance, R_t describes the ohmic losses of the tag, L_t and L_r the inductances of the tag and reader, and C_t the capacitance of the tag antenna setup.
The tag capacitance C_t (see Fig. 1.3), the tuning capacitance C_t' added to the parasitic capacitance C_p, combined with the tag inductance L_t lead to a certain resonance frequency of the tag. C_t' is used to set the resonance frequency to a certain value, because C_p and L_t are tied to the chip and antenna design. A resonance frequency higher than 13.56 MHz is chosen because multiple tag antennas can be in the reader field, which increases the capacitive load, and leads to a lower resonance frequency. A typical value would be 15 MHz [8].
With the given CM of the tag, which is shown in Fig. 1.3, the quality factor Q of the tag can be calculated [8]:

$$Q = \frac{1}{\frac{R_t}{\omega \cdot L_t} + \frac{\omega \cdot L_t}{R_L}}. \tag{1.5}$$

The Q factor is an indication for the resonant voltage/current step-up. By

[3] $\omega = 2 \cdot \pi \cdot f$

maximizing it the induced voltage in the tag increases, which leads to a higher operating range. By contrary, maximizing the Q factor also narrows the bandwidth, which leads to a higher sensitivity of the system with respect to component tolerances. Furthermore, a narrow bandwidth also decreases the ability to have multiple tags in the reader field. This means a trade-off has to be made regarding operating range versus reliability.

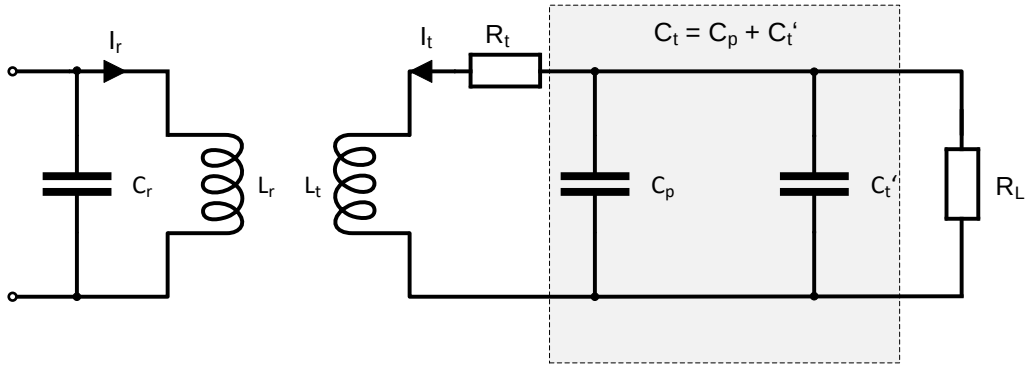

Figure 1.3: The CM for the reader antenna coil and the tag, which consists of coil antenna and microchip: This CM can be used to determine the operating range and to maximize the reliability of the HF RFID system [8].

1.1.2 Communication

The communication between the reader and tag is performed by modulation of the magnetic field. The reader-to-tag and tag-to-reader communication can take place simultaneously (full-duplex procedure) as well as one by one (half-duplex procedure) [8].

The so-called forward link is the reader sending data to the tag. The tag sending data to the reader is called backward link. To understand the backward link it

is crucial to grasp the electrical behavior of the tag seen from the reader. The reader does experience an additional load Z_t' (see Fig.1.4), if an resonant tag is brought into the reader field. This load can be influenced even more if a load resistor on the tag side is switched on and off, which is basically amplitude modulation [8]. The data from the backward link can have an up to 80 dB smaller amplitude than the forward link signal. Thus, modulation sidebands need to be utilized. These are created by amplitude modulation with, e.g., a transistor, by switching on and off the above mentioned load resistor at a high elementary frequency (e.g. $f_s = 212\,\text{kHz}$, 424 kHz or 848 kHz). The modulated sidebands do exist now at f_{reader} (usually 13.56 MHz) $\pm f_s$. The backward link can now be detached from the forward link with a bandpass and amplified to be read out [8]. In Fig. 1.4, Z_t', the reader supply voltage U_r, and the load modulation field effect transistor (FET) T_t are shown. In this particular case, the drain-source resistance of T_t is used as a load resistor [8].

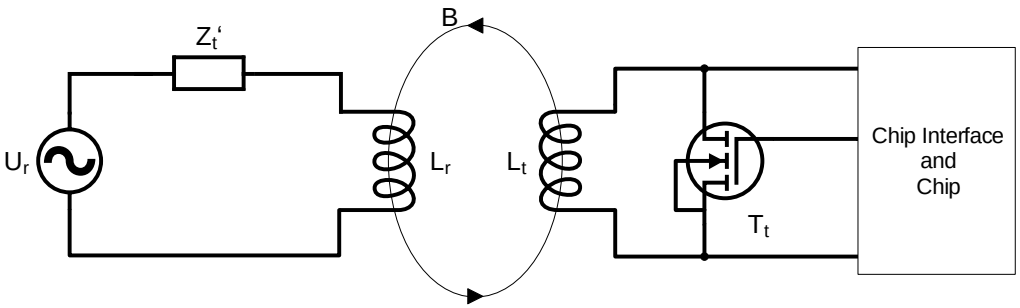

Figure 1.4: Basic principles of RFID load modulation [8]: In this figure, the important components for load modulation are shown. Z_t' is not a component of the reader antenna circuit, it is there to model the electrical influence of the resonant tag in the near field, which can be represented by a load. This load is influenced by the drain-source resistance of the FET T_t .

1.2 Sensor Tags

After having explained the basic principles of RFID tags, the focus will now be on RFID sensor tags and their problems regarding disturbance robustness as well as on the disturbance robustness of capacitive sensors.

1.2.1 Tamper Tag

In this section the properties of a specific RFID sensor tag (NTAG 213 TT), provided by NXP Semiconductors, are summarized [16] . This sensor tag is a predecessor of possible future capacitive sensor tags, for whose development this master thesis is providing a disturbance model. The novelty of the new product will be that the sensor reads out the status of a capacitance instead of a wire loop.

The NTAG 213 TT reads out the status of a wire loop to generate a binary 1-bit output. The wire loop is placed outside of the sensor and therefore requires two extra pins (detection pin (DP) and the chip ground (GND), see Fig. 1.5). Some applications of an RFID sensor tag with such a wire loop (tag tamper feature) are product authentication (e.g. detect the manipulation of a wine bottle closure) and smart packaging (e.g. manipulating a package destroys the wire, which is detected by the sensor) [16, P.3].
The main building blocks of the NTAG 213 TT are displayed in Fig. 1.5.
The radio frequency (RF) interface consists of [16]:

- A modulator,
- A demodulator,
- A rectifier,
- A clock generator,
- A power-on reset (POR), and
- A voltage regulator.

The modulator and demodulator are needed to modulate the magnetic field (see Sec. 1.1.2) to send data to the reader and to demodulate the data received from the reader. In addition, a rectifier and clock generator are required to supply the chip with a proper clock signal. The POR gets triggered at the beginning of each interrogation phase. Afterwards the tag switches to its idle state and is ready to be addressed by the reader.
The voltage regulator keeps the voltage in the defined boundaries to ensure a proper voltage supply for the chip (see Sec. 1.1.1)[16].
The digital control unit (DCU) consists of an electrically erasable programmable read-only memory (EEPROM) Interface and an anticollision block. This block, in combination with the POR and the idle sate, ensures a proper data transfer if more than one tag is present in the reader interrogation field. The EEPROM serves as a configuration/manufacturer data storage as well as a readable and

writeable memory for the user [16].

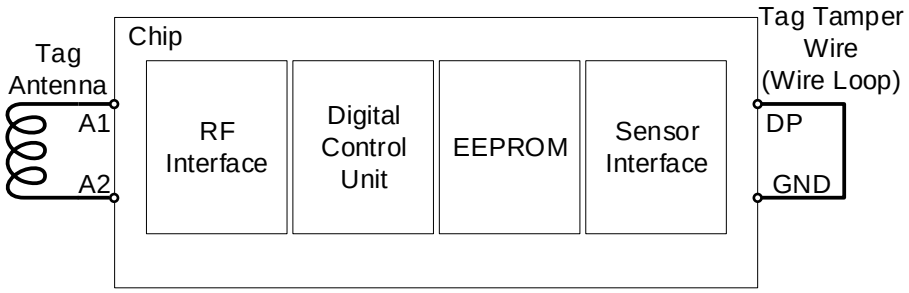

Figure 1.5: The blocks included in an RFID sensor tag with a wire loop (tag tamper feature) [16]: A1 and A2 are antenna pins, DP the detection pin and GND is the chip ground.

Disturbance Robustness

The wire loop is a 1-bit sensing element. The logical state of the sensor depends on the state of the wire loop. It can be either a closed wire loop or an open wire loop, i.e., causing a short circuit or an open circuit between the DP and GND [16]. The binary state of the sensor tag does experience disturbances due to parasitic coupling with the reader antenna in its near field. The wire loop couples inductively with the reader antenna in case of the short circuit and couples capacitively with the reader antenna in case of the open circuit. The short circuit case is analyzed in the following. In Tab. 1.1 the results of an analytical calculation of the induced wire loop voltage V_{ind} are shown for a wire loop with a loop area A (see Fig. 1.6). The chosen magnetic field strength $H = 1.5\,\frac{\text{A}}{\text{m}}$ and $H = 7.5\,\frac{\text{A}}{\text{m}}$ are the minimum and maximum allowed values for according to the ISO10373 $-$ 6 standard [17].

V_{ind} can be calculated with [8]:

$$V_{\text{ind}}(t) = -\frac{d\psi(t)}{dt} = \mu_o \cdot A \cdot \omega \cdot \sqrt{2} \cdot H \cdot \sin(\omega \cdot t)$$

$$V_{\text{ind}}(t) = \sqrt{2} \cdot V_{\text{ind}} \cdot \sin(\omega \cdot t) \Rightarrow V_{\text{ind}} = \mu_o \cdot A \cdot \omega \cdot H \tag{1.6}$$

with

$$\psi(t) = \mu_o \cdot H(t) \cdot A\,, \;\; H(t) = \sqrt{2} \cdot H \cdot \cos(\omega \cdot t) \;\text{ and }\; \omega = 2 \cdot \pi \cdot f_{\text{HF}}\,.$$

Here, ω is the angular frequency, $f_{\text{HF}} = 13.56\,\text{MHz}$ the HF RFID frequency, $\psi(t)$ the magnetic flux through the wire loop, H the magnetic field strength at the wire loop (no distance between tag and reader), μ_o the permeability of air, and A the area of the wire loop.

In contrast, the open-circuited wire loop is modeled by two different capacitance values $C_{\text{loop}} = 0.1\,\text{pF}$ and $C_{\text{loop}} = 0.5\,\text{pF}$. Two different values are chosen because the exact capacitive value of the open circuit is not known and 0.1 pF to 0.5 pF is the estimated range, in which C_{loop} is expected. The capacitance value C does not affect the coupled voltage V_{coupling} in the schematic shown in Fig. 1.7. Only the asymmetry factor p and C_{loop} do influence V_{coupling}. The simulation results of the coupling network (see Fig. 1.7) are shown in Tab. 1.2.

By comparing Tab. 1.1 and Tab. 1.2 one can see that the capacitive influence can be larger than the inductive influence. This supports the claim that parasitic capacitive coupling to capacitive sensing elements is an issue and needs to be understood.

$H\,(\frac{\mathrm{A}}{\mathrm{m}})$	$A\,(\mathrm{cm}^2)$	$V_{\mathrm{ind}}\,(\mathrm{V})$
1.5	2	0.064
1.5	6	0.58
7.5	2	0.32
7.5	6	2.89

Table 1.1: V_{ind} calculated based on the reader magnetic field strength H and on the loop area A. The values in this table are root mean square values.

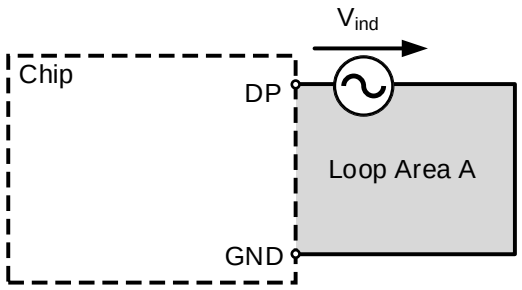

Figure 1.6: Parasitic inductive coupling effect: Voltage induced at the wire loop due to the magnetic field of the reader and the wire loop area A.

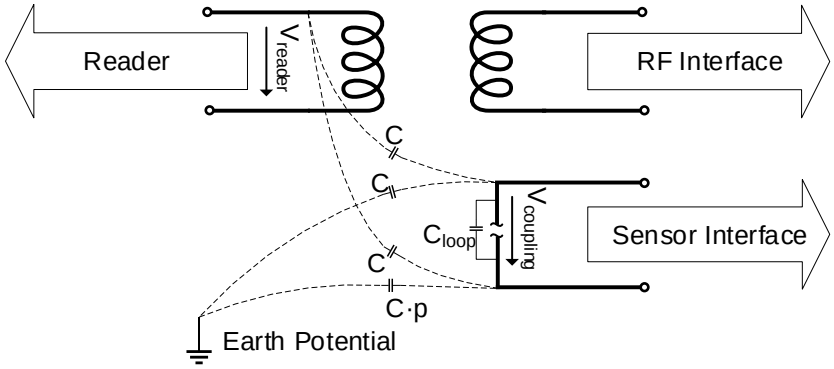

Figure 1.7: Parasitic capacitive coupling from a reader antenna to an open-circuited wire loop: The coupling is modeled with a symmetric capacitance network. p introduces an asymmetry in the network, which is in combination with C_{loop} responsible for V_{coupling}. For the RF interface see Sec. 1.2.1. and Fig. 1.5 $V_{\text{reader}} = 50\,\text{V}$ is the voltage applied to the reader antenna.

p	$V_{\text{coupling}}\,(\text{V})$ for $C_{\text{loop}} = 0.1\,\text{pF}$	$V_{\text{coupling}}\,(\text{V})$ for $C_{\text{loop}} = 0.5\,\text{pF}$
1	0.00	0.00
0.9	1.18	0.86
0.5	7.38	5.21
0.1	17.69	11.87

Table 1.2: V_{coupling} simulated based on the capacitance asymmetry factor p and the open-circuited wire loop capacitance C_{loop}. $V_{\text{reader}} = 50\,\text{V}$ is the voltage applied to the reader antenna. The values in this table are root mean square values.

1.2.2 Robust Capacitive Sensors

In this section the focus lies on dealing with interferences, which are influencing capacitive sensors, rather than understanding their electrical behavior.
As mentioned earlier, very few research results regarding capacitive sensors in combination with RFID tags have been published so far. A general research result about robust capacitive sensors is documented in prior published literature [4], which is outlined in the following paragraphs.
Usually small signal levels as well as bad signal-to-noise ratios are the main challenges for capacitive sensors. Hence a housing, which removes the problem of electrical contamination, can also operate as electromagnetic shield against interferences. In many areas, like RFID tags, such a housing is not available for cost and space efficiency reasons [4].
A possible first step towards dealing with the robustness issues is to use a ratiometric measurement principle. This improves the signal-to-noise ratio and deals with problems occurring due to very small signal levels. This principle makes the current sensor output additionally a function of prior sensor outputs [4].
To cope with electrical conducting contamination, which causes leakage currents, low impedance sensors are used. This ensures very little impact of high-ohmic parasitics. Furthermore, a technique called frequency hopping can be utilized. Here the signal, which measures the capacitance, operates with different frequencies. In general, disturbances have a high power or a narrow bandwidth, which means that there can be a lot of advantages to frequency hopping. Nevertheless, a wider bandwidth to increase the frequency hopping range deals better with interfering signals but causes also a worse signal-to-noise ratio [4].

LC Resonator

Texas Instruments [20] introduced an LC Resonator, also called LC tank, to greatly reduce the noise floor and to ensure a high immunity against electromagnetic interference. The capacitance of the capacitive sensing element is read out via a capacitance-to-digital converter (FDC). Here, the capacitance C forms a resonant circuit with an inductance L and its resonance frequency is measured by the FDC. This ensures low influences of interfering signals, since the capacitance is measured by a frequency measurement instead of a current measurement, which is more susceptible to these interfering signals [7].

1.3 Thesis Outline

In the following, I provide a short outline of the thesis. Since this thesis is aimed as a guideline for circuit designers, a CM for parasitic capacitive coupling is the desirable result. This is due to the fact that a CM, once determined, can be implemented efficiently in a circuit simulator as, for example, Cadence Virtuoso [21]. In Chap. 2 a CM for HF RFID antennas is developed and the electromagnetic simulation environment CST [18] is verified by comparing measurement, simulation, and analytical results of typical HF RFID antennas. In Chap. 3 I use the prior established CM for HF RFID antennas to create an extended model that emulates a specific reader antenna, a specific capacitive sensing element, and their parasitic capacitive coupling network. I derived a methodology so that this extended model can be created consistently. This methodology is the major output of this thesis, because it can be applied to different coils. In Chap. 4, I give an overview about the most important results of the thesis and an outlook for possible future work.

2 Antenna System Modeling

In this chapter, a general CM for a coil is introduced and is verified by measurements and electromagnetic simulations. The comparison of CM, measurement, and simulation results verifies additionally the electromagnetic simulation environment CST. In addition, the CM allows the comparison with theory and analytically calculated results of it. A further verification step is the comparison of the mutual inductance and the coupling coefficient between the two-port measurements, simulations and analytical calculations (see Sec. 2.3, Fig. 2.5). The International Organization for Standardization (ISO) $10373-6$ standard defines the geometry of the coils as well as the measurement setup. It includes the proximity coupling device (PCD) (see Fig.2.1), which is the reader coil, a calibration coil (CC) (see Fig.2.2), a device under test (DUT), and two Helmholtz coils for field measurements at specific positions of the DUT [17]. From this ISO setup, the PCD and CC are used for the verification of CST and the validation of the CM.

2.1 Electromagnetic Model

In CST MWS it is advised to use the frequency domain solver when sweeping over a large frequency range, which includes resonances of circuits [19]. If the frequency is high enough and therefore the penetration depth is much smaller than the thickness of the conductors, 'lossy' metal can be chosen for the conductors of the coils (see Fig. 2.1 and 2.2). This reduces the simulation time significantly [19]. In the case of the ISO $10373-6$ standard, coils with a copper

thickness of 35 µm are used. Thus, a frequency higher than roughly 90 MHz is required. Since the simulations are starting at 300 kHz and the frequency region of interest for later simulations is the HF RFID frequency (13.56 MHz), 'normal' copper has to be used to increase the accuracy of the simulations at the cost of simulation time [18]. CST also has an integrated circuit simulator and an optimizer tool. For complex circuit simulations the program AWR [3] is used. The validity of both circuit simulators and the optimizer tool have been verified before. This means that the determining factor of which one to use is time efficiency versus convenience.

Fig. 2.1 and 2.2 show the coils, which are used for the verification in Chap. 2, from the ISO test setup. Fig. 2.3 shows the the two coils from Fig. 2.1 and 2.2 mounted on the so-called ISO tower.

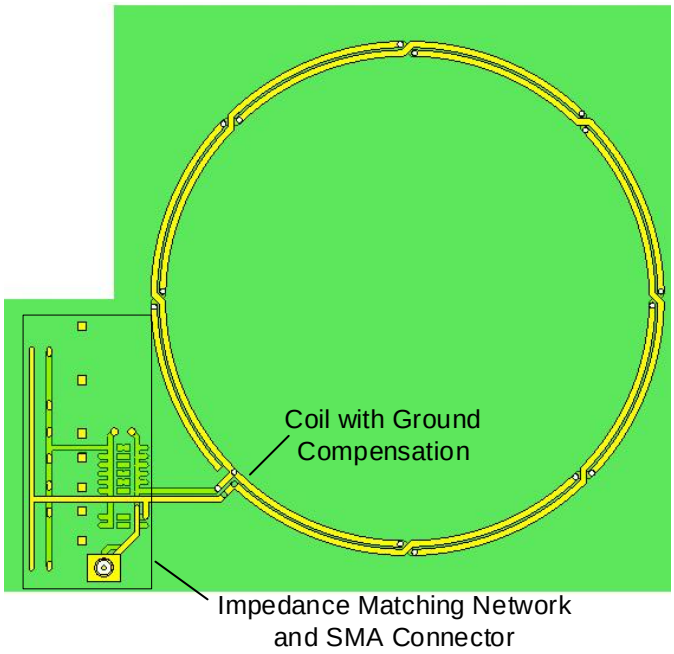

Figure 2.1: Layout of the PCD coil including the ground compensation coil: The coil is connected with an SMA connector to the ports of the VNA for measurements and the virtual ports of CST for simulations. The coil geometry parameters are listed in the following: radius = 75 mm, copper thickness = 35 µm, copper width = 1.8 mm.

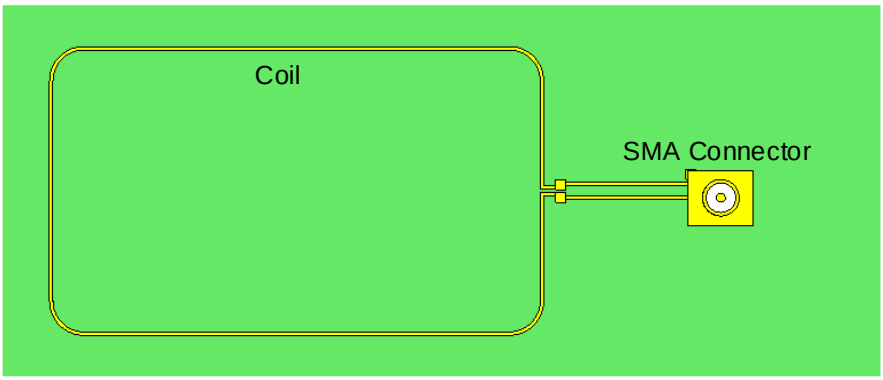

Figure 2.2: Layout of the CC: The coil is connected with an SMA connector to the ports of the VNA for measurement and the virtual ports of CST for simulation. The coil geometry parameters are listed in the following: length = 72 mm, width = 42 mm, copper thickness = 35 µm, copper width = 0.5 mm, edge radius = 0.5 mm.

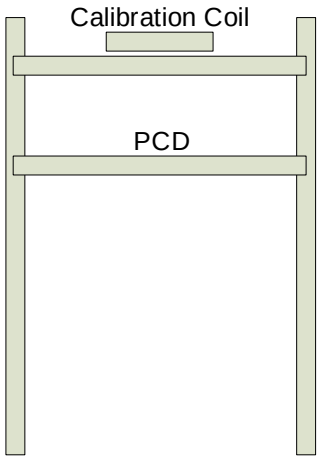

Figure 2.3: Geometry of the ISO 10373 – 6 standard tower: In this schematic only the PCD and the CC (representing the tag antenna) are included. This is sufficient, because with these two coils all necessary verification steps for CST can be accomplished.

2.2 Circuit Model

The electrical behavior of a coil can be described with a CM (see Fig.2.4, [9]). Here, R_{skin} is the lumped element, a resistance, modeling the skin effect. R_{DC} is the resistance of the coil at low frequencies. L is the inductance of the coil. C is the parasitic capacitances of the coil. [9].

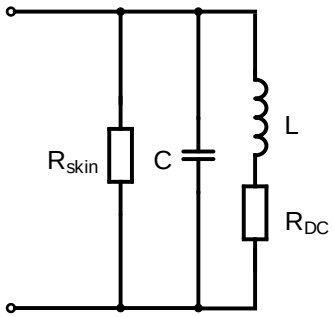

Figure 2.4: Four lumped element CM of a coil [9]: This CM is valid until a frequency of roughly 1.5 times than the resonance frequency of the coil [9].

2.3 Analytical Calculations

In this section R_{DC} and L are calculated analytically for the CC and PCD as well as M and k between the two. From here on indices 'CC' signal a variable regarding the CC, and indices 'PCD' signal a variable regarding the PCD. Furthermore, some analytical calculations are done for conductors of the coils, hence variables regarding these conductors carry the indices 'c'.
By knowing the conductivity ρ ($1.72 \cdot 10^8 \frac{\Omega}{\text{m}}$ for annealed copper), the length l,

and the area A of an conductor, the resistance can be calculated with [15]:

$$R = \frac{\rho \cdot l}{A}. \tag{2.1}$$

The inductance of a circular coil with a cylindrical conductor can be calculated by knowing the radius r of the loop, the radius of the conductor r_c, and the permeability μ of the surrounding material with [6]:

$$L = 4 \cdot \pi \cdot r \cdot (\ln(\frac{8 \cdot r}{r_c}) - 2)^1. \tag{2.2}$$

In a system, consisting of two coils, the coupling coefficient k can be calculated with Eq. 1.2. When both coils are circular and in a coaxial arrangement, parallel and sharing the same axis through the center, M can be calculated by knowing the radius r_1 and r_2 of the coils, the distance between the coils d, the permeability μ, and the first order ($F(c)$) and second order ($E(c)$) elliptical integral with [11]:

$$M = \frac{2 \cdot \mu}{c} \cdot \sqrt{r_1 \cdot r_2} \cdot [(1 - \frac{c^2}{2}) \cdot F(c) - E(c)] \tag{2.3}$$

and

$$c = \frac{4 \cdot r_1 \cdot r_2}{[(r_1 + r_2)^2 + d^2]}.$$

As mentioned above the formulas for L and M are approximations and require circular coils with cylindrical conductors. As shown in Fig. 2.2 the CC has a rectangular shape and in Fig. 2.1 it is shown that the PCD does not have a perfect circular shape. Furthermore, the coils are printed on a printed circuit board (PCB) and the traces have a rectangular cross section. The deviations of the PCD coil shape are neglected but the rectangular cross section of the

[1] r, r_c in cm, L in nH

conductors as well as the rectangular shaped CC are transformed into the shape of a circle with the same area, to simplify the calculations. A rectangle with the length a, the width b and hence an area of A can be transformed into a circle with the same area A. r, the radius of the circle, is then calculated with:

$$r = \sqrt{\frac{A}{\pi}} = \sqrt{\frac{a \cdot b}{\pi}}. \tag{2.4}$$

a_{CC} mm	b_{CC} mm	$a_{c,CC}$ mm	$b_{c,CC}$ µm	$a_{c,PCD}$ mm	$b_{c,PCD}$ µm
72	42	0.5	35	1.8	35

r_{CC} mm	r_{PCD} mm	$r_{c,CC}$ µm	$r_{c,PCD}$ µm	$l_{c,CC}$ mm	$l_{c,PCD}$ mm
31.03	74.5	74.64	141.61	278	518.1

Table 2.1: Analytically calculated coil geometries: The length of the PCB trace l consists of the perimeter and the distance (50 mm) from the SMA connector to the coil.

2.4 Measurements and Simulations

Fig. 2.5 (a) shows the measurement setup for a single coil, Fig. 2.5 (b) shows the measurement setup for transmission impedances. The port of the vector network analyzer (VNA) is connected to the coil with a coaxial cable and a sub-miniature version A (SMA) connector. Prior to the measurements the VNA has to be calibrated to set the reference plane of the measurement device directly to the input of the coil. This allows the measurement of the input

impedance of the coil directly at its input port, i.e., the SMA connector. In simulations the port is defined directly at the SMA connector to facilitate an accurate comparison with the measurement. The two coils investigated are shown in Fig. 2.1 and 2.2.

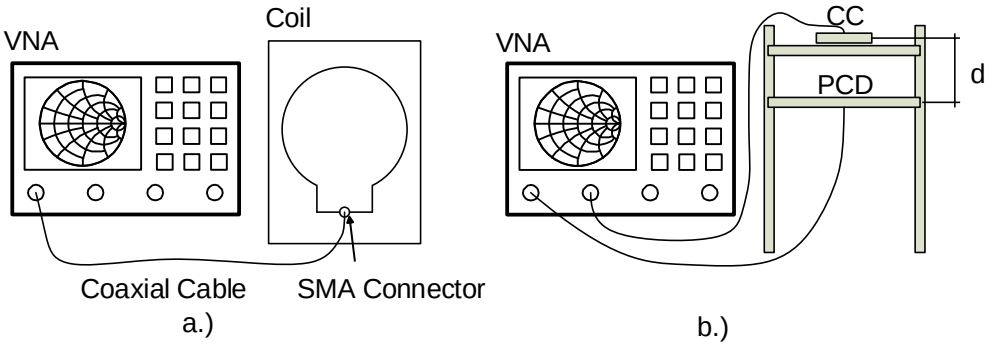

Figure 2.5: Setups for coil measurements: (a) The picture on the right shows the input impedance measurement setup. (b) The picture on the right presents the setup to measure the transmission impedances between two coils.

2.4.1 Extraction of Lumped Elements

All formulas of the extraction method in this section can be found in [13] and [14]. Both measurement and simulation result in input impedances over a frequency range, hence the extraction method of the CM is exactly the same. L and R_{DC} require the input impedance (Z_{11}) to be measured at lower frequency (e.g. 1MHz), due to R_{skin} and C being high ohmic and therefore having almost no impact. Thus, R_{DC} and L and are calculated with:

$$R_{\mathrm{DC}} = Re(Z_{11}),\ L = \frac{Im(Z_{11})}{\omega}. \tag{2.5}$$

At resonance frequency f_{res} the imaginary part of Z_{11} is zero. With that knowledge, f_{res} can be read out from a Z_{11} plot. In addition, the formula for f_{res}, for the circuit shown in Fig. 2.4, is:

$$f_{\text{res}} = \frac{1}{2\pi \cdot \sqrt{L \cdot C}}. \tag{2.6}$$

In Eq. 2.6 the influences of R_{DC} and R_{skin} can be neglected. This was verified with simulation results. Thus, this simplified formula can be used to calculate C with f_{res} and L by:

$$C = \frac{1}{(2 \cdot \pi \cdot f_{\text{res}})^2 \cdot L}. \tag{2.7}$$

Further, the real part of Z_{11} is equal to the skin effect resistance at f_{res}:

$$R_{\text{skin,@fres}} = Re(Z_{11,\text{@fres}}). \tag{2.8}$$

Due to the $\frac{1}{\sqrt{f}}$[2] proportionality of R_{skin}, the skin effect over the whole frequency range is known:

$$R_{\text{skin,@fx}} = R_{\text{skin,@fres}} \cdot \sqrt{\frac{f_{\text{res}}}{f_{\text{x}}}}. \tag{2.9}$$

Now all lumped elements for Fig.2.4 are known.

[2]This influence on the absolute value of input impedances is negligible. The difference is 0.1 ‰ at HF frequency and 10 ‰ at $1.33 \cdot f_{\text{res}}$ for the PCD and CC.

2.5 Comparison of Results

The curve shapes of measurements and simulations are very similar. Only the absolute values show differences, which is to be expected. This is due to the fact that the VNA is inaccurate at open circuit (resonance frequency) and short circuit (low frequency) measurements, which are the regions in which the lumped element values are determined. Further, the geometry values of the coils in the simulations are varied by $\pm$ 5% and resulted in almost no deviation from the original values. This shows that the results are almost independent to manufacturing tolerances of the PCB.
In the following plots the indices 'm' signifies measurement results, while 's' signifies simulation results. Furthermore, the CM can be calculated with values gathered from measurements denoted with the indices 'mc' or with values from the simulation denoted by 'sc'.

2.5.1 Lumped Elements and Input Impedances

Fig. 2.6, 2.7, 2.8 and 2.9 show a very good alignment of the CM to its simulation/measurement results. In addition, the analytical calculation, measurement, and simulation results show a good agreement. This comparison verifies the electromagnetic simulation environment CST, which is used, from now on, in the following investigations.

	$R_{DC,CC}$ mΩ	L_{CC} nH	$f_{res,CC}$ MHz	$R_{skin,@fres,CC}$ kΩ	C_{CC} pF
Analytical calc.	241.0	238.57	–	–	–
Measurement	246.9	260.95	193.75	6.08	2.59
Simulation	270.52	208.88	227.33	21.80	2.35

Table 2.2: Comparison of lumped elements of the CC found by analytical calculations, measurements, and simulations.

	$R_{DC,PCD}$ mΩ	L_{PCD} nH	$f_{res,PCD}$ MHz	$R_{skin,@fres,PCD}$ kΩ	C_{PCD} pF
Analytical calc.	176.0	594.41	–	–	–
Measurement	163.05	495.94	43.47	5.30	27.03
Simulation	184.04	493.13	45.47	4.17	24.84

Table 2.3: Comparison of lumped elements of the PCD found by analytical calculations, measurements, and simulations.

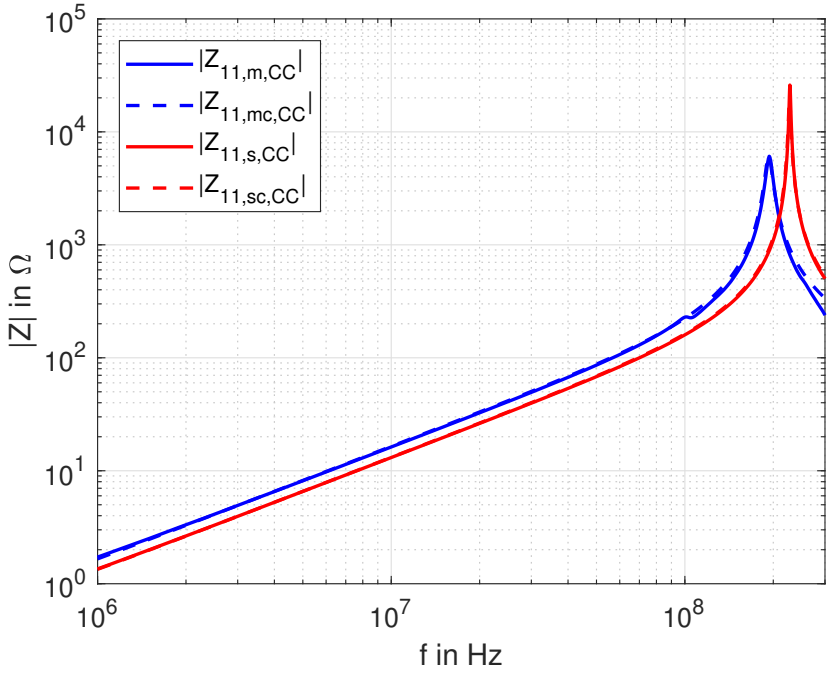

Figure 2.6: Absolute value of the input impedance versus frequency of the CC coil: The plot shows a comparison of measurement and simulation results, which have a good agreement.

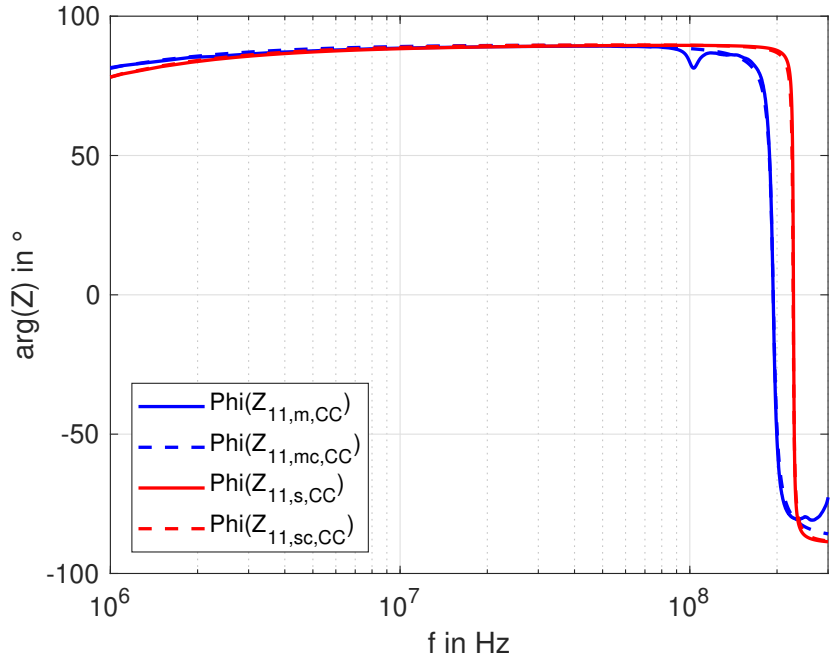

Figure 2.7: Phase of the input impedance versus frequency of the CC coil: The plot shows a comparison of measurement and simulation results, which have a good agreement. The ripple of Phi$(Z_{11,\mathrm{m,CC}})$ at 100 MHz is either caused by the measurement setup or due to the high frequency measurements. At lower frequencies such a distortion is not present (see Fig. 2.9).

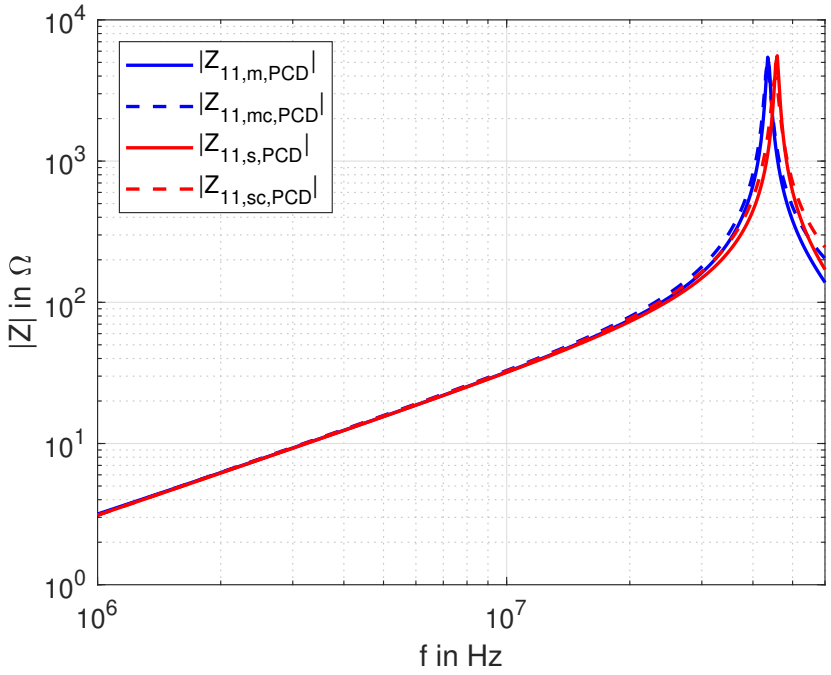

Figure 2.8: Absolute value of the input impedance versus frequency of the PCD coil: The plot shows a comparison of measurement and simulation results, which have a good agreement.

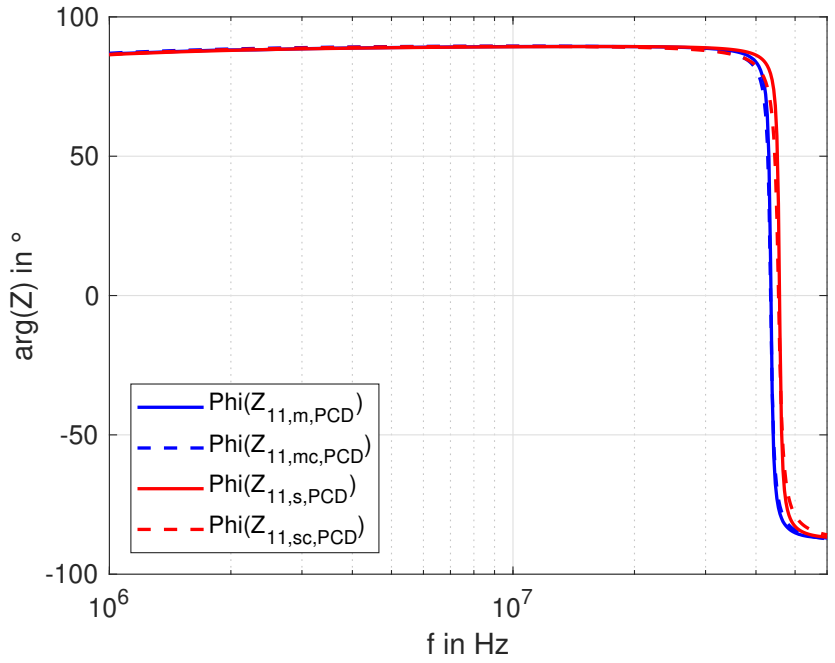

Figure 2.9: Phase of the input impedance versus frequency of the PCD coil: The plot shows a comparison of measurement and simulation results, which have a good agreement.

2.5.2 Coupling Coefficients and Mutual Inductances

The measurements of the coupling coefficients are compared over several distances d (see Fig. 2.5 (b)) of the coils. Similar to the one port investigations, the two port investigations also have a good agreement. This means that the two port simulations can be trusted as well. In Fig. 2.11 and Fig. 2.10 the indices 'c' signal analytically calculated results. The mutual inductance can be calculated from the transmission impedance Z_{12} with [12]:

$$M = \frac{Im(Z_{12})}{\omega}. \tag{2.10}$$

	d (cm)	3.75	7.5	10	15
Analytical calc.	M (nH)	18.03	8.51	5.20	2.18
	k (10^{-3})	47.79	22.59	13.80	5.78
Measurement	M (nH)	16.13	7.31	4.44	0.92
	k (10^{-3})	44.82	20.32	12.33	2.55
Simulation	M (nH)	18.74	8.28	4.99	2.08
	k (10^{-3})	58.27	25.75	15.52	7.93

Table 2.4: Results for the mutual inductance and the coupling factor calculated based on analytical, measurement, and simulation results.

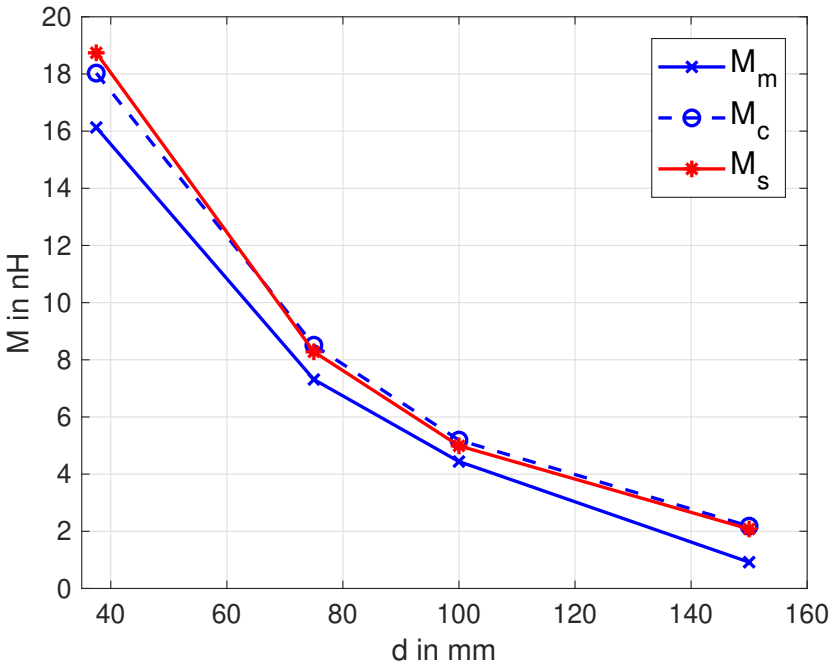

Figure 2.10: Mutual inductance versus distance between the CC and PCD: The plot shows a comparison of measurement, simulation, and analytical results, which have a good agreement. The deviation of the measurement results from simulation and analytical results can be explained by a non-perfect measurement setup and not perfectly aligned coil centers.

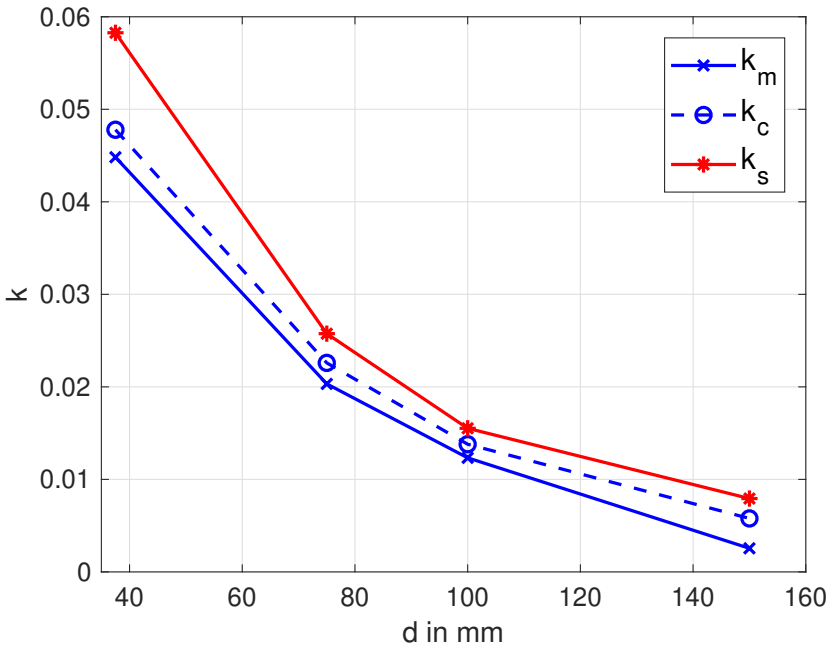

Figure 2.11: Coupling factor versus distance between the CC and PCD: The plot shows a comparison of measurement, simulation, and analytical results, which have, in general, a good agreement. As expected, the coupling factor decreases with distance (see Sec. 1.1.1).

3 Parasitic Capacitive Coupling Model

After the verification of the simulation environment, the main objective of this thesis is approached, i.e., the modeling of parasitic capacitive coupling between a coil and a capacitive sensing element with a CM. As a first step, a simple circular coil with two electrodes in its center is created. These two electrodes represent the capacitive sensing element (electrode capacitance). This setup is called test coil (TC) from now on. With the TC, the methodology to determine the electrical behavior of parasitic capacitive coupling between a reader coil and an electrode capacitance is established.

3.1 Methodology

The general methodology to generate a CM for parasitic capacitive coupling between a coil and an electrode capacitance is listed in detail in the following:

- Create an EM,
- Determine the input and transmission impedances of the EM;
- Find a CM, which aligns with the input and transmission impedances of the EM;
- Perform a parameter sweep of the lumped elements of the CM to find a parameter combination, which leads to the global minimum of the difference between the CM and EM input and transmission impedances;
- Optimize lumped elements with the CST optimizer to further align

transmission impedances.

Fig. 3.1 shows the geometry of the TC setup.

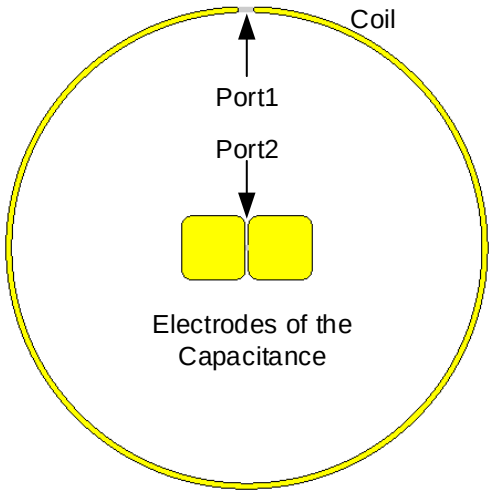

Figure 3.1: Geometry of the TC setup: This picture shows a circular coil and two planar electrodes which represent an electrode capacitance. The geometry parameters are listed in the following: radius = 75 mm, copper thickness = 35 µm, copper width = 1.8 mm, width of the square electrodes = 35 µm.

As in Chap. 2, the lumped elements for the coil of the TC setup need to be determined. In addition, the electrode capacitance $C_{e,TC}$ of the planar electrodes is calculated with the input impedance of Port 2 (see Fig. 3.2) by the formula:

$$C_{e,TC} = \frac{1}{\omega \cdot Im(Z_{22,EM,TC})}. \tag{3.1}$$

Furthermore, a coupling network needs to be established as well. Here, a very simple, and as seen later, sufficient capacitance network is chosen. This

network consists of two coupling capacitances $C_{1,TC}$ and $C_{2,TC}$. Throughout this whole chapter indices 'TC' are used to denote a variable belonging to the TC. Input and transmission parameters with indices 'CM' belong to the CM and with the indices 'EM' belong to the EM.
The lumped elements discussed in the paragraph above, are in the following combined into the CM shown in Fig. 3.2. This CM is used as an electrical description of the EM going forward.

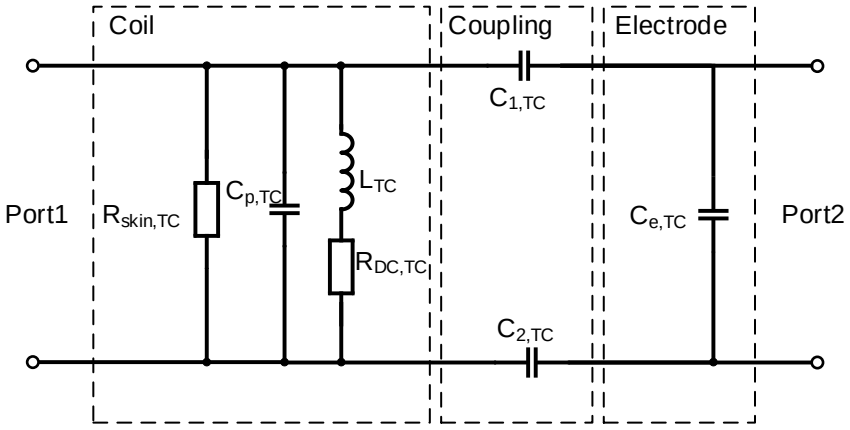

Figure 3.2: CM of the TC setup: This schematic shows the lumped elements modeling the coil, the coupling network, and the electrode capacitance.

With the input impedances ($Z_{11,EM,TC}$ and $Z_{22,EM,TC}$) and the procedure form Sec. 2.4.1 and Eq. 3.1 all lumped elements, except $C_{1,TC}$ and $C_{2,TC}$, of the CM can be determined. The results are shown in Tab. 3.1.

3.1.1 Parasitic Coupling Capacitances

Table 3.1 does not include parasitic coupling capacitances $C_{1,TC}$ and $C_{2,TC}$. These capacitances are included in $C_{e,TC}$ and $C_{p,TC}$, which are calculated from

$R_{DC,TC}$	L_{TC}	$f_{res,TC}$	$R_{skin,@fres,TC}$	$C_{p,TC}$	$C_{e,TC}$
mΩ	nH	MHz	kΩ	pF	pF
175.6	473.41	301.04	34.270	0.5904	0.787

Table 3.1: Lumped element values of the TC: This table shows the lumped elements for the coil and electrode capacitance of the TC CM (see Fig. 3.2).

input impedances of the already coupled EM (see Fig. 3.1). This means, that when determining $Z_{11,EM,TC}$ the resonance frequency is influenced by the $C_{e,TC}$ and vice versa. To find the correct values for all the capacitances in the CM the CST optimizer and the circuit simulator AWR [3] are used. First, because of the geometry, the condition

$$C_{1,TC} = C_{2,TC} = C_{c,TC} \tag{3.2}$$

is introduced. This condition allows the CST optimizer to align $\mathrm{Im}(Z_{12,CM,TC})$ with $\mathrm{Im}(Z_{12,EM,TC})$ by guessing values for $C_{c,TC}$ faster. The result for this first approximation is $C_{c,TC} \approx 30\,\mathrm{fF}$.

Now $C_{c,TC}$, $C_{p,TC}$ and $C_{e,TC}$ are approximately known. To get more accurate values a parameter sweep is performed in AWR with the parameter ranges shown in Table 3.2.

The AWR educational license allows up to 10^6 calculations per simulation. Since 1001 frequency steps are used per input and transmission impedances, no more than 999 different parameter combinations are allowed. This leads to specific numbers of steps chosen for the capacitances, with $C_{e,TC}$ being the least influential on the transmission impedance.

	min pF	*max* pF	*steps*
$C_{c,TC}$	0.025	0.045	11
$C_{p,TC}$	0.52	0.6	11
$C_{e,TC}$	0.73	0.80	8

Table 3.2: Parameter ranges for the parameter sweep: In this table the capacitance value ranges and number of steps for each capacitance are shown, resulting in 968 different parameter combinations, which leads to 968 different input and transmission impedances.

3.1.2 CM Optimization

Cost Function

The fitting quality of the CM to the EM has to be quantified for each parameter combination so that the problem at hand can be optimized. Thus, a cost function (CF) is introduced (see Eq. 3.3 and 3.4). First, the real parts of input and transmission impedances are neglected due to the fact that the imaginary parts are roughly one to two magnitudes larger than the real parts. To introduce a proper optimization method, the influence of each capacitance has to be understood. On the one hand $C_{p,TC}$ and $C_{e,TC}$ influence the general curvature as well as the resonance frequency of $\mathrm{Im}(Z_{12,CM,TC})$ and on the other hand $C_{c,TC}$ influences the offset of $\mathrm{Im}(Z_{12,CM,TC})$ at lower frequencies. Thus the CF is generated for 2 different frequency ranges: 5 MHz to $1.33 \cdot f_{res}$ ($CF_{1,12}$) and 5 MHz to $0.5 \cdot f_{res}$ ($CF_{2,12}$), which leads to the following equations:

$$CF_{1,12} = \sum_{f=5\,MHz}^{1.33 \cdot f_{res}} (Im(Z_{12}(f)_{CM}) - Im(Z_{12}(f)_{EM})); \tag{3.3}$$

$$CF_{2,12} = \sum_{f=5\,MHz}^{0.5 \cdot f_{res}} (Im(Z_{12}(f)_{CM}) - Im(Z_{12}(f)_{EM})). \tag{3.4}$$

In Eq. 3.3 and 3.4 the differences of all frequency points in the given frequency range are summed up. The same goes for Im($Z_{11,CM}$) ($CF_{1,11}$, $CF_{2,11}$) and Im($Z_{22,CM}$) ($CF_{1,22}$, $CF_{2,22}$). With the prior results the general cost functions for the whole system (CF_1 and CF_2) can be calculated with:

$$CF_1 = CF_{1,11} \cdot CF_{1,12} \cdot CF_{1,22}\,;\; CF_2 = CF_{2,11} \cdot CF_{2,12} \cdot CF_{2,22}. \tag{3.5}$$

Cost Function Interpolation

Each cost function (CF_1, CF_2) is summarized in the respective cost function matrix ($CF_{1,m}$, $CF_{2,m}$) with the dimensions 11x11x8. The resolution of the parameter sweep is increased by interpolating the matrices, which leads to the dimensions 101x101x71. The interpolation has to reviewed to ensure its validity, which can be done by visual inspection of its results in plots. $CF_{1,m}$ and $CF_{2,m}$ are 3D matrices, which means a 4D plot would be needed to plot the cost functions versus $C_{p,TC}$, $C_{p,TC}$ and $C_{e,TC}$. Thus, the problem is split into two steps. First, the parameter values related to the minimum of $CF_{1,m}$ are determined. The logarithm of $CF_{1,m}$ is now plotted (see Fig.3.3) versus $C_{p,TC}$ and $C_{e,TC}$ for the prior determined $C_{c,TC}$ value.
The values for $C_{p,TC}$ and $C_{e,TC}$ are now known and $C_{c,TC}$ can be determined by finding the minimum of $CF_{2,m}$. Fig. 3.4 shows the logarithm of $CF_{2,m}$ versus $C_{c,TC}$.
These parameter sweeps and calculations lead to the capacitance values shown in Tab. 3.3.

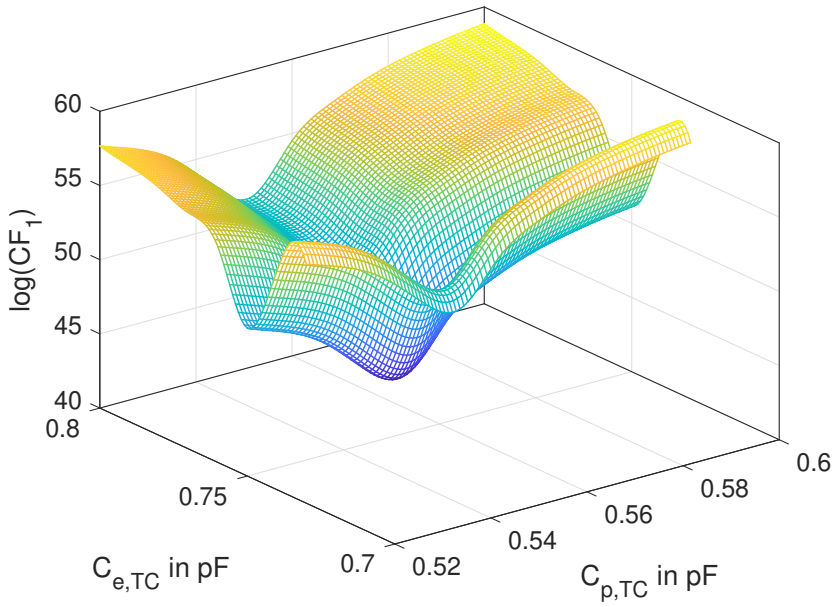

Figure 3.3: Interpolated cost function $CF_{1,\mathrm{int,TC}}$ versus $C_{\mathrm{p,TC}}$ and $C_{\mathrm{e,TC}}$: This picture shows the influence of $C_{\mathrm{p,TC}}$ and $C_{\mathrm{e,TC}}$ on the alignment between the CM and EM calculated by $CF_{1,\mathrm{int,TC}}$. A minimum of $C_{1,\mathrm{int,TC}}$ is clearly visible for the capacitance values $C_{\mathrm{p,TC}}$ and $C_{\mathrm{e,TC}}$ shown in Tab. 3.6.

$C_{\mathrm{c,TC}}$ pF	$C_{\mathrm{p,TC}}$ pF	$C_{\mathrm{e,TC}}$ pF
0.0332	0.5592	0.76

Table 3.3: Lumped element results accomplished with interpolation and the cost function: These results lead to the global minimum difference between the CM and EM of the TC, which was determined with the help of the cost functions $CF_{1,\mathrm{TC}}$ and $CF_{2,\mathrm{TC}}$ (see Eq. 3.3, 3.4 and 3.5).

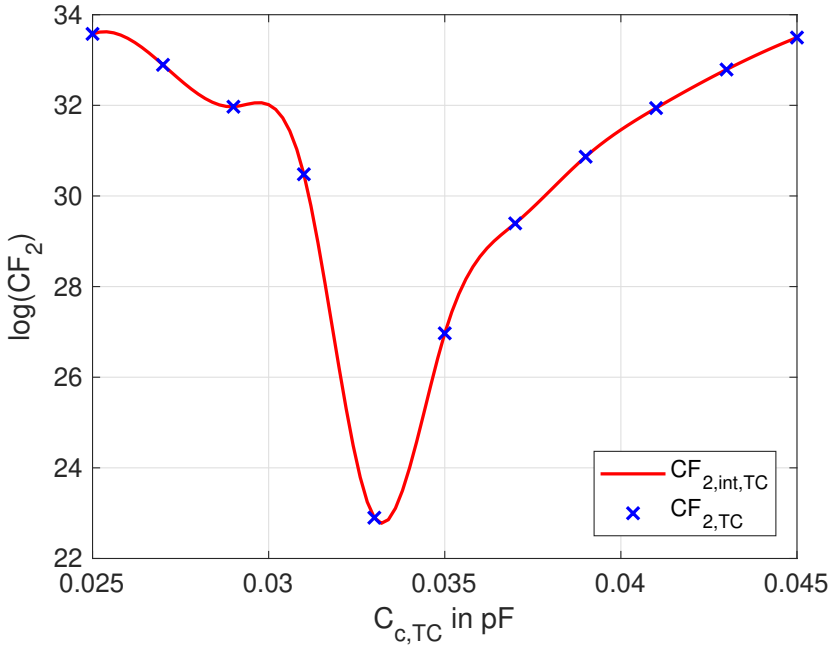

Figure 3.4: Interpolated cost function $CF_{2,\mathrm{int,TC}}$ and cost function $CF_{2,\mathrm{TC}}$ versus $C_{\mathrm{c,TC}}$: This picture shows the influence of $C_{\mathrm{c,TC}}$ on the alignment between the CM and EM calculated by $CF_{2,\mathrm{int,TC}}$ and $CF_{2,\mathrm{TC}}$. A minimum of $CF_{2,\mathrm{int,TC}}$ is clearly visible for the capacitance value $C_{\mathrm{c,TC}}$ shown in Tab. 3.6.

3.1.3 Fine Optimization with CST

The final part of the optimization is done with the CST optimizer tool. In Sec. 3.1.2 values are approximated for $C_{c,TC}$, $C_{p,TC}$ and $C_{e,TC}$ with all input and transmission impedances being taken into account. This analysis proves that the current values belong not only to a local but a general minimum. Thus, the CST optimizer can be used to generate more accurate results, which can be trusted. The lumped elements from Tab. 3.3 are varied ($\pm$2% around results from Tab.3.3) to generate a minimum for Eq. 3.3 and 3.4, which means that in this step only the transmission impedances are taken into account. This results in a good overall alignment and in a very good transmission impedance alignment as shown in Fig. 3.5 and 3.6. $C_{p,TC}$ and $C_{e,TC}$ are used to minimize $CF_{1,12}$ and $C_{c,TC}$ is used to minimize $CF_{2,12}$. This optimization results in the values shown in Tab. 3.4.

The capacitance values from Table 3.4 lead to $\mathrm{Im}(Z_{12,CM,TC})$ shown in Fig.3.5 and the percentage error between $\mathrm{Im}(Z_{12,CM,TC})$ and $\mathrm{Im}(Z_{12,EM,TC})$ shown in Fig. 3.6.

$C_{c,TC}$ pF	$C_{p,TC}$ pF	$C_{e,TC}$ pF
0.03363	0.5704	0.7752

Table 3.4: Lumped element results accomplished with the CST optimizer: These results lead to the minimum difference between the transmission impedances of the CM and EM of the TC, which was determined with the help of the cost functions $CF_{1,12,TC}$ and $CF_{2,12,TC}$ (see Eq. 3.3 and 3.4).

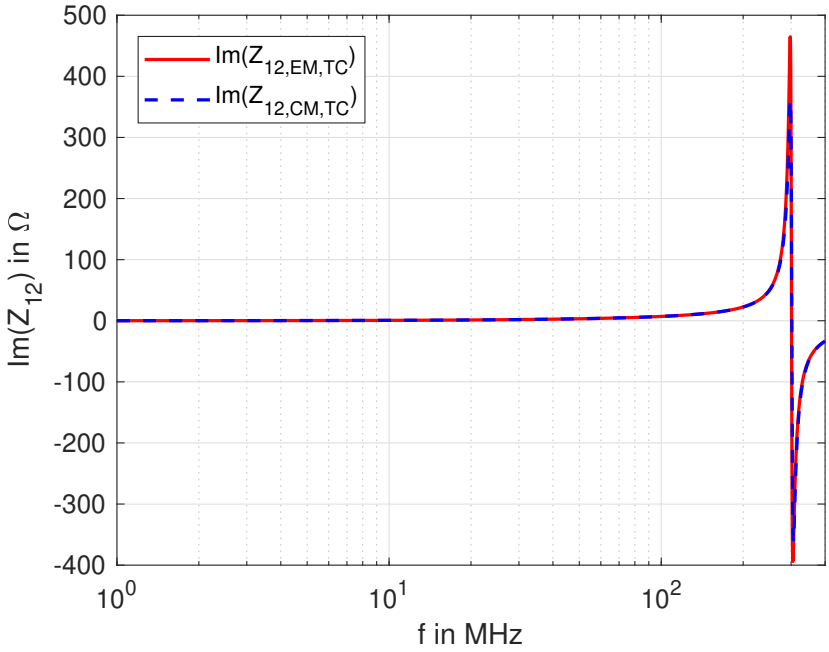

Figure 3.5: $\mathrm{Im}(Z_{12,\mathrm{CM,TC}})$ and $\mathrm{Im}(Z_{12,\mathrm{EM,TC}})$ versus frequency: This picture compares the transmission parameter of the EM with CM, which have a good agreement. The real parts of the transmission impedances are not relevant, because they are one to two magnitudes smaller than the respective imaginary parts.

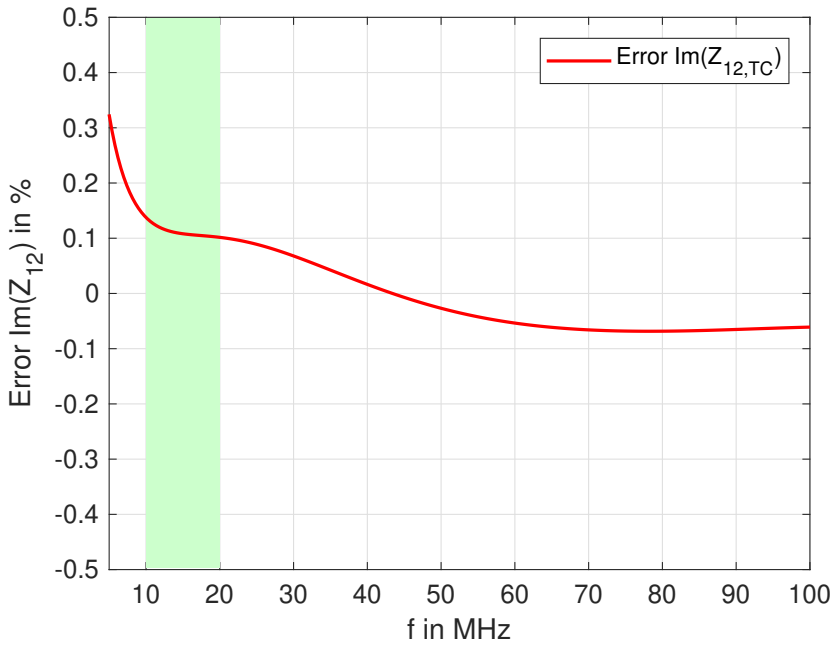

Figure 3.6: Difference between $\mathrm{Im}(Z_{12,\mathrm{CM,TC}})$ and $\mathrm{Im}(Z_{12,\mathrm{EM,TC}})$ versus frequency in percent: The relative error is calculated as follows $\frac{\mathrm{Im}(Z_{12,\mathrm{EM,TC}})-\mathrm{Im}(Z_{12,\mathrm{CM,TC}})}{\mathrm{Im}(Z_{12,\mathrm{EM,TC}})} \cdot 100\,\%$. The green area is marking the HF RFID relevant frequency range of 10 MHz to 20 MHz.

Discussion

As shown in Fig. 3.5 the general curvature is very well aligned by the CM with the chosen parameter values for the capacitances $C_{\mathrm{c,TC}}$, $C_{\mathrm{p,TC}}$ and $C_{\mathrm{e,TC}}$. This is achieved by optimizing $C_{\mathrm{p,TC}}$ and $C_{\mathrm{e,TC}}$ versus a different frequency range than $C_{\mathrm{c,TC}}$. Furthermore, the aligning error between the CM and the EM is less than 0.3%, which confirms that the coupling can be modeled very well by using two parasitic coupling capacitances with the symmetry condition of both being equal to each other. With these results one can also be confident to approach the PCD, a more complex coil, of the ISO tower and get a reasonable good alignment with this simple parasitic capacitive coupling network.

3.2 PCD Model

After deriving a methodology to create an accurate CM to model parasitic capacitive coupling between the reader antenna and the sensing capacitance, this methodology is now applied to a more complex coil, i.e., the PCD of the ISO-10373-6 standard [17], with the exact same electrode capacitance as shown in Fig. 3.1. Here, the lumped elements and variables are labeled with 'PCD' to signal that they are PCD related.

The same CM, as shown in Fig. 3.2, is used [13].

For this setup new lumped element parameters have to be determined. For

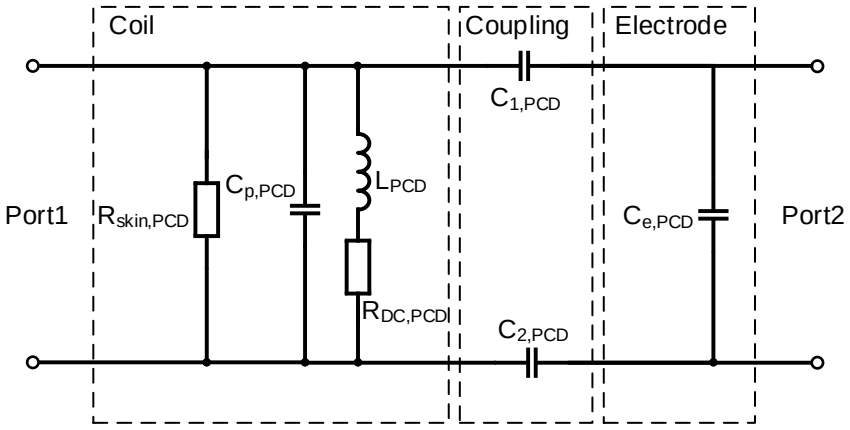

Figure 3.7: CM of the PCD (see Fig. 2.1) setup: This schematic shows the lumped elements modeling the coil, the coupling network, and the electrode capacitance.

this calculations the same geometry condition as for the TC is used: $C_{1,\mathrm{PCD}} = C_{2,\mathrm{PCD}} = C_{c,\mathrm{PCD}}$. The results are shown in Tab. 3.5. The values show slight deviations to the PCD discussed in Tab. 2.3 because the impedance matching network and the SMA connector were excluded so that only the coil itself has to be modeled.

As the next step, interpolated logarithmic plots of CF_1 and CF_2 are created

$R_{DC,PCD}$	L_{PDC}	$f_{res,PCD}$	$R_{skin,@fres,PCD}$	$C_{p,PCD}$	$C_{e,PCD}$
mΩ	nH	MHz	kΩ	pF	pF
215.8	478.23	49.213	5.527	21.87	1.082

Table 3.5: Lumped element values of the PCD: This table shows the lumped elements for the coil and electrode capacitance of the PCD CM (see Fig. 3.7).

and shown in Fig. 3.8 and 3.9. Again, very distinct global minima are found, which belong to the parameter values shown in Tab. 3.6.
By implementing the values of the capacitances from Tab. 3.6 in the CM and optimizing the alignment between $\mathrm{Im}(Z_{12,CM,PCD})$ and $\mathrm{Im}(Z_{12,EM,PCD})$, with the CST optimizer, the results from Tab. 3.7 are achieved.
These results lead to the relative error shown in Fig. 3.10. The error is larger in comparison to the error of the TC model. This increase of error can be explained with the larger parasitic capacitance $C_{p,PCD}$. A small absolute error of $C_{p,PCD}$ has much less impact on the cost function and resonance frequency than the same absolute error of the parasitic TC capacitance $C_{p,TC}$. This means that, a small error has basically no influence on $CF_{1,PCD}$, but a large influence on $CF_{2,PCD}$, which is not the case for $CF_{1,TC}$ and $CF_{2,TC}$. One indication of this reasoning can be seen by comparison of Fig. 3.8 and Fig. 3.3. Here, Fig. 3.8 shows a less steep slope parallel to the C_p axis for the C_e value determined in Tab. 3.6 and 3.3, than Fig. 3.3 does.
By going through the optimization steps (see Sec. 3.1), a difference between the CM transmission impedances and the EM transmission impedances of less than 0.3% (5 MHz to 100 MHz) is accomplished for the TC. For the PCD a difference of less than 1% (10 MHz to 20 MHz) is accomplished. This means that one can determine accurate lumped elements for the given CM with the developed methodology.

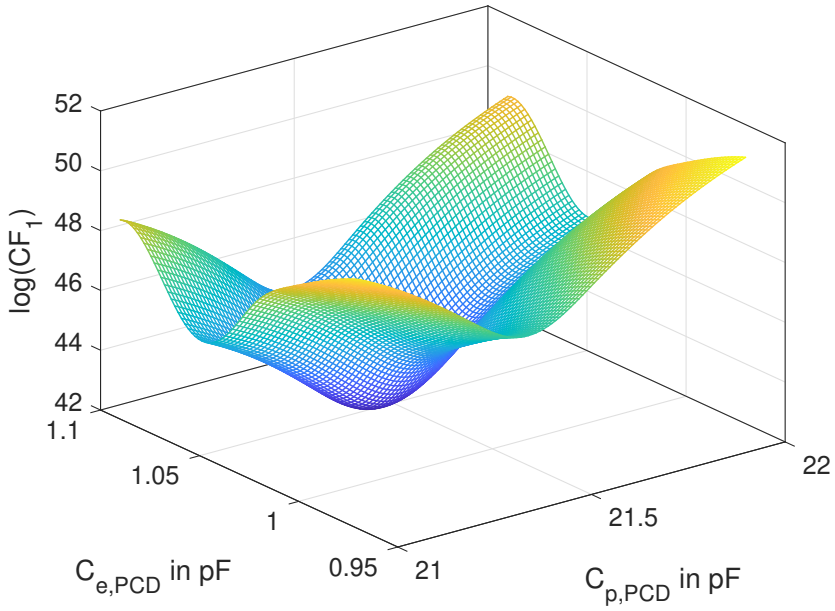

Figure 3.8: Interpolated cost function $CF_{1,\mathrm{int,PCD}}$ versus $C_{\mathrm{p,PCD}}$ and $C_{\mathrm{e,PCD}}$: This picture shows the influence of $C_{\mathrm{p,PCD}}$ and $C_{\mathrm{e,PCD}}$ on the alignment between the CM and EM calculated by $CF_{1,\mathrm{int,PCD}}$. A minimum of $C_{1,\mathrm{int,PCD}}$ is clearly visible for the capacitance values $C_{\mathrm{p,PCD}}$ and $C_{\mathrm{e,PCD}}$ shown in Tab. 3.6.

$C_{\mathrm{c,PCD}}$ pF	$C_{\mathrm{p,PCD}}$ pF	$C_{\mathrm{e,PCD}}$ pF
0.04	21.45	1.056

Table 3.6: Lumped element results accomplished with interpolation and the cost function: These results lead to the global minimum difference between the CM and EM of the PCD, which was determined with the help of the cost functions $CF_{1,\mathrm{PCD}}$ and $CF_{2,\mathrm{PCD}}$ (see Eq. 3.3, 3.4 and 3.5).

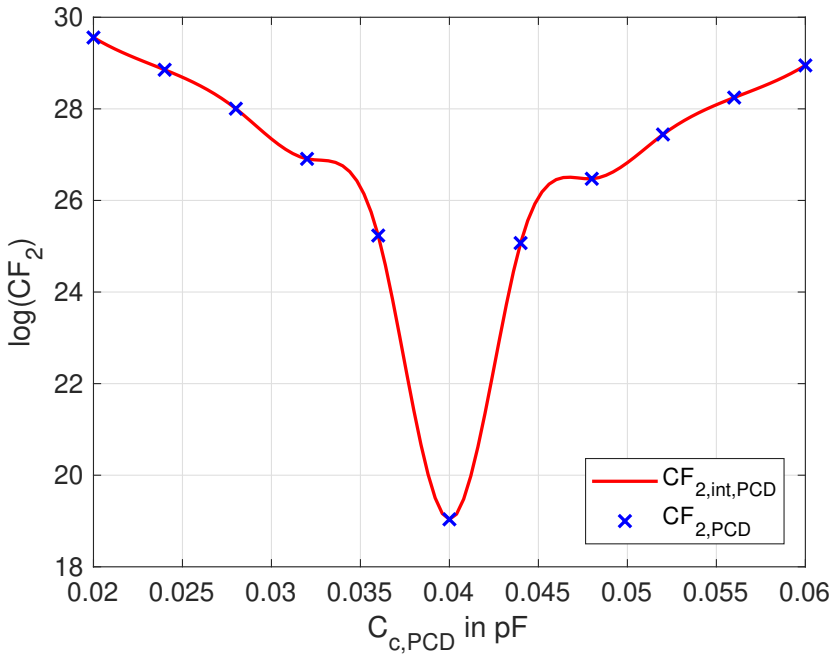

Figure 3.9: Interpolated cost function $CF_{2,\mathrm{int,PCD}}$ and cost function $CF_{2,\mathrm{PCD}}$ versus $C_{\mathrm{c,PCD}}$: This picture shows the influence of $C_{\mathrm{c,PCD}}$ on the alignment between the CM and EM calculated by $CF_{2,\mathrm{int,PCD}}$ and $CF_{2,\mathrm{PCD}}$. A minimum of $CF_{2,\mathrm{int,PCD}}$ is clearly visible for the capacitance value $C_{\mathrm{c,PCD}}$ shown in Tab. 3.6.

$C_{\mathrm{c,PCD}}$ pF	$C_{\mathrm{p,PCD}}$ pF	$C_{\mathrm{e,PCD}}$ pF
0.0408	21.621	1.057

Table 3.7: Lumped element results accomplished with the CST optimizer: These results lead to the minimum difference between the transmission impedances of the CM and EM of the PCD, which was determined with the help of the cost functions $CF_{1,12,\mathrm{PCD}}$ and $CF_{2,12,\mathrm{PCD}}$ (see Eq. 3.3 and 3.4).

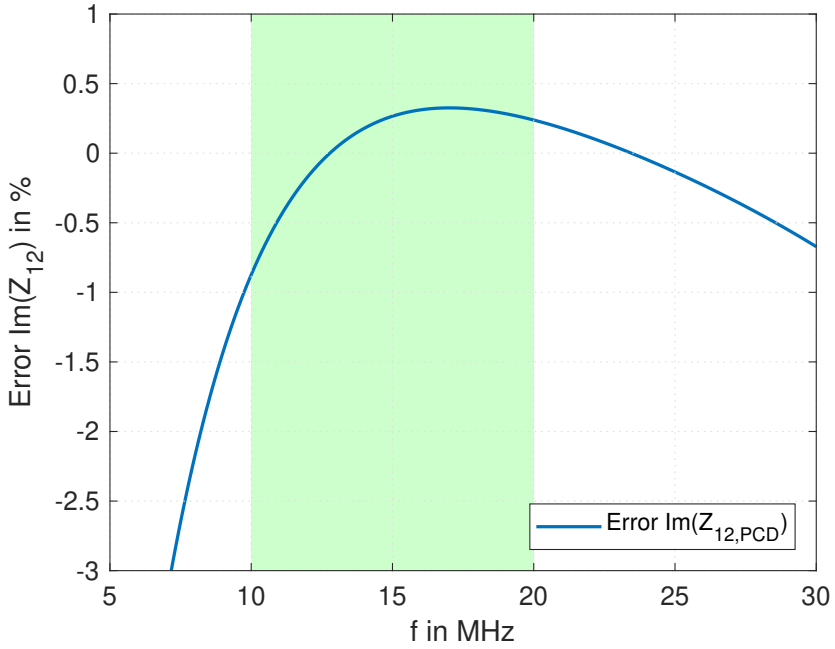

Figure 3.10: Difference between $\mathrm{Im}(Z_{12,\mathrm{CM,PCD}})$ and $\mathrm{Im}(Z_{12,\mathrm{EM,PCD}})$ versus frequency in percent: The relative error is calculated as follows $\frac{\mathrm{Im}(Z_{12,\mathrm{EM,PCD}})-\mathrm{Im}(Z_{12,\mathrm{CM,PCD}})}{\mathrm{Im}(Z_{12,\mathrm{EM,PCD}})} \cdot 100\,\%$. The green area is marking the HF RFID relevant frequency range of 10 MHz to 20 MHz.

4 Conclusions

In this thesis, I investigate parasitic capacitive coupling between high frequency (HF) radio frequency identification (RFID) reader antennas and capacitive sensing elements attached to HF RFID passive sensor tags. I have analyzed this issue for the specific case of a sensor tag connected to a capacitance, i.e., two planar metal parts located next to each other. The analysis is primarily done with the simulation software CST. I created an electromagnetic model (EM) of a basic reader antenna - tag capacitance system. Since the results of this thesis are targeted at circuit designers, I described the electrical behavior of the EM with a circuit model (CM). The goal was to align the input and transmission impedances of the CM and EM as best as possible, with a focus on the transmission impedances.

I derived a methodology to achieve this alignment with the help of a very simplistic electromagnetic model (see Fig. 3.1). It was shown, that already a very basic parasitic capacitive coupling network does yield a good alignment of the CM and EM (see Fig. 3.2). Larger differences of the transmission impedances do occur at lower frequencies ($\leq 5\,\text{MHz}$), which is due to the fact that CST has issues to calculate the transmission impedances at lower frequencies correctly [19]. This issue can be taken into account and is not a problem, because the frequency of interest is 13.56 MHz. By going through the optimization steps (see Sec. 3.1) a difference between the CM transmission impedances and the EM transmission impedances of less than 0.3% (5 MHz to 100 MHz) is accomplished.

For a more complex reader antenna, the proximity coupling device (PCD) from

the ISO 10373 – 6 [17], the results are worse. The higher parasitic capacitance of the PCD can be held accountable for the worse results. The same relative error of the parasitic capacitance has a larger influence on the parasitic coupling capacitances of the PCD than on the parasitic coupling capacitances of the TC. This leads to a difference of less than 1% from 10 MHz to 20 MHz, which is still a very good description of the electrical behavior.

In future work one can try to determine a CM for different distances and angles between the coil and capacitance. Different antennas would also be interesting to characterize, but would probably require more complex CMs of the coils due to capacitances between loops or, e.g., substrate losses.

Bibliography

[1] Fotopoulou et. al. "Wireless Power Transfer in Loosely Coupled Links: Coil Misalignment Model." In: *IEEE Transactions on Magnetics* vol. 2.no. 2 (2011) (cit. on p. 1).

[2] I. Lee et al. "Circuit Techniques for Miniaturized Biomedical Sensors." In: *Proceedings of the IEEE 2014 Custom Integrated Circuits Conference*. Sept. 2014, pp. 1–7 (cit. on p. 2).

[3] AWR. *National Instruments*. URL: `https://www.awrcorp.com/` (cit. on pp. 18, 39).

[4] G. Brasseur. "Design Rules for Robust Capacitive Sensors." In: *IEEE Transactions on Instrumentation and Measurement* vol. 52.no. 4 (2003), pp. 1261–1265 (cit. on p. 15).

[5] Z. Tan; R. Daamen; A. Humbert; Y. V. Ponomarev; Y. Chae and M. A. P. Pertijs. "A 1.2-V 8.3-nJ CMOS Humidity Sensor for RFID Applications." In: *Journal of Solid-State Circuits* vol. 10.no. 10 (2013), pp. 2469–2477 (cit. on p. 2).

[6] N. Cooke. "Self-Inductance of the Elliptical Loop." In: *Proceedings of the Institution of Electrical Engineers* vol. 110.issue 7 (1963), pp. 1293–1298 (cit. on p. 23).

[7] TI Sensor FDC2114. *Texas Instruments*. URL: `http://www.ti.com/lit/ds/symlink/fdc2114.pdf` (cit. on p. 16).

[8] K. Finkenzeller. *Fundamentals and Applications in Contactless Smart Cards, Radio Frequency Identification and Near-Field Communication*. John Wiley and Sons Ltd., 2010 (cit. on pp. 1–9, 12).

[9] M. Gebhart. *RFID-Systems Vorlesung, Testverfahren*. 2011. URL: http://rfid-systems.at/08_Testverfahren_2011.pdf (cit. on p. 22).

[10] J. Van Rethy; G. Gielen. "An Energy-Efficient Capacitance-Controlled Oscillator-Based Sensor Interface for MEMS Sensors." In: *2013 IEEE Asian Solid-State Circuits Conference (A-SSCC)*. Nov. 2013, pp. 405–408 (cit. on p. 2).

[11] H.C. Miller. "Inductance Formula for a Single-Layer Circular Coil." In: *Proceedings of the IEEE* vol. 75.issue 2 (1987), pp. 256–257 (cit. on p. 23).

[12] Dae-Hee Weon; Saeed Mohammadi. "High Performance 3-D Helical RF Transformers." In: *2007 IEEE/MTT-S International Microwave Symposium* (2007) (cit. on p. 33).

[13] T. Bauernfeind; W. Renhart; S. Schemthanner; M. Gebhart; K. Preis. "Equivalent Circuit Parameter Extraction for Controlled Detuned NFC Antenna Systems Utilizing Thin Ferrite Foils." In: *Telecommunications (ConTEL), 2013 12th International Conference on* (2013) (cit. on pp. 25, 47).

[14] C. Scherabon. *How to Model the ISO Tower*. 2014 (cit. on p. 25).

[15] W. Plaßmann; D. Schulz. *Handbuch Elektrotechnik - Grundlagen und Anwendungen für Elektrotechniker*. Springer Vieweg, 2012 (cit. on p. 23).

[16] NXP Semiconductors. *NTAG 213 TT - NFC T2T Compliant IC with Tag Tamper Feature*. 2017. URL: http://nxp.com (cit. on pp. 1, 9–11).

[17] International Standard. *Identification Cards — Test Methods — Part 6: Proximity Cards*. Jan. 2015 (cit. on pp. 11, 17, 47, 53).

[18] CST Studio Suite. *Germany: CST Computer Simulation Technology*. SP5 2017 (cit. on pp. 16, 18).

[19] CST Support. *Simulation Accuracy*. Private Communication. 2018 (cit. on pp. 17, 52).

[20] TI. *Texas Instruments*. URL: http://www.ti.com/ (cit. on p. 16).

[21] Cadence Virtuoso. *Cadence Design Systems Inc.* URL: https://www.cadence.com (cit. on p. 16).